ACS OMEGA

Open Access

http://pubs.acs.org/journal/acsodf

Article

Graphite-Based Localized Heating Technique for Growing Large Area Methylammonium Lead Bromide Single Crystalline Perovskite Wafers and Their Charge Transfer Characteristics

Mano Balaji Gandhi, Aiswarya Mohan, Sreekala Meyyarappallil Sadasivan, Sabu Thomas, Angappane Subramanian, Jean Christian Bernède, Guy Louarn, Linda Cattin,* and Predeep Padmanabhan*

Cite This: *ACS Omega* 2025, 10, 10220−10229

Read Online

ACCESS | Metrics & More | Article Recommendations | Supporting Information

ABSTRACT: Development of a reproducible technique to grow large area single crystalline perovskite wafers is an open research gap in the field of single crystalline perovskite solar cells. A graphite-based localized heating technique for growing large area methylammonium lead bromide ($CH_3NH_3PbBr_3$; MAPBr) single crystalline thin film (SCTF) on different buffer layers, such as glass/indium doped tin oxide (ITO), glass/ITO/poly(triaryl amine) (PTAA), and glancing angle deposition (GLAD) coated glass/ITO/TiO_2 substrates is reported, and their charge transport properties are discussed. It is observed that the localized heating technique can confine the supersaturation of the precursor mainly to the center of the substrate, leading to a restricted number of nucleations within a specific area on the substrate. Here, such 2−3 seed crystals obtained initially are allowed to grow to a larger size of up to 65 mm^2. The X-ray diffraction (XRD) analysis indicated that the large area SCTF is an actual single crystal and not a heterogeneous group of small crystals merged together with a crystallinity index (CI) of 92.60 ± 0.11% which was comparable to that of the bulk single crystal (97.74 ± 0.47%). The atomic force microscopy (AFM) image depicted a smooth SCTF surface (R_a = 4.37 ± 0.01 nm), and the wave-like pattern is attributed to the substrate morphology, implying that the topography of the substrate plays a crucial role in obtaining a planar SCTF. The XRD, UV−visible, photoluminescence (PL), Raman, and FTIR spectra analyses revealed that the large area SCTF is phase pure and free of residual impurities. The charge injection characteristics of the SCTFs grown on different buffer layers were investigated using PL emission (PLE) and PL decay analyses. The decrease in the PLE intensity for the SCTFs grown on PTAA and TiO_2 substrates implied exciton quenching behavior, indicating the injection of the photogenerated charge carriers into the charge transfer layers (CTLs). The decrease of the fast decay component from τ_1 = 4.77 ± 0.18 ns for glass to τ_1 = 3.32 ± 0.07 ns for TiO_2 and τ_1 = 3.15 ± 0.33 ns for PTAA is ascribed to the interfacial recombination of the charges accumulated at the CTL/perovskite interface. These results propose that the localized heating technique can be employed for growing large area single crystalline perovskite wafers for optoelectronic and photovoltaic device applications.

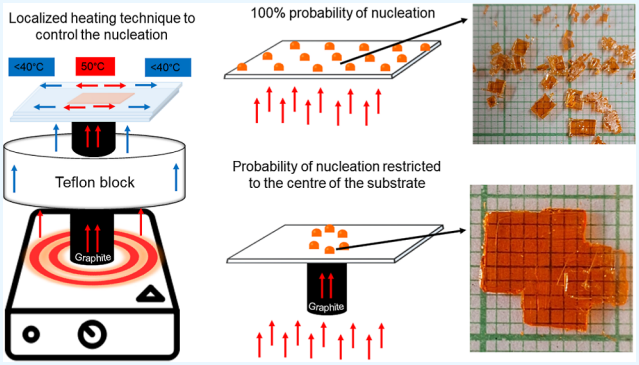

1. INTRODUCTION

Single crystalline perovskite solar cells (SC-PSCs) are emerging as significant competitors to the polycrystalline thin film PSCs. The SC-PSCs have a huge advantage of zero grain boundaries which reduces the loss of the photogenerated charge carriers due to recombination at the grain boundaries.[1−3] This can, theoretically, boost the power conversion efficiency (PCE) toward the Schottky−Queisser limit.[4,5] Several research reports are available on the development of SC-PSCs[6,7] with high efficiencies.[8−18] These results signify that SC-PSCs demonstrate great potential to surpass polycrystalline thin film-based PSCs.

Several techniques have been developed and employed for the growth of hybrid lead halide perovskite-based single crystalline thin films (SCTFs). Chen et al. reported the growth of methylammonium lead bromide ($CH_3NH_3PbBr_3$; MAPBr) SCTFs using a temperature gradient method.[19] Two cleaned glass substrates were clipped together and immersed in the

Received: October 18, 2024
Revised: February 24, 2025
Accepted: February 26, 2025
Published: March 4, 2025

precursor solution, and the solution was heated from the bottom. Crystallization starts due to the temperature gradient, and the capillary action resulted in the free flow of the precursor from the bottom to top, resulting in continuous crystal growth. MAPBr SCTF with thicknesses ranging from 40 nm to 140 μm were grown. Monocrystalline MAPBr thin films with an average thickness of 30 μm were grown using cavitation triggered asymmetrical crystallization technique by Peng et al.[20] The MAPBr precursor was filled in a crystallizing dish which was placed inside a larger dish containing dichloromethane antisolvent. This entire setup was placed in an ultrasonic bath, and short ultrasonic pulse of <1 s was applied to induce supersaturation resulting in crystal growth. Rao et al. employed a space confined method to control the thickness of the MAPBr SCTF by introducing a PTFE spacer to control the film thickness. The substrate was heated locally from the center while the precursor was continuously pumped between the substrates. Wang et al. developed 35 μm-thick MAPI single crystalline wafer using a geometry-regulated dynamic-flow reaction system. In this work, two substrates were sandwiched together with a spacer in between which defines the crystal wafer thickness. The substrates were then placed in a crystallizing dish which is heated from the bottom and fresh MAPI precursor is pumped between the substrates.[21] Chen et al. developed a hydrophobic interface-confined lateral crystal growth method for the growth of 10 μm-thick MAPI SCTF, using poly(triaryl amine) (PTAA) as the hydrophobic as well as the hole transporting layer (HTL). The perovskite precursor was dropped at one end of the sandwiched indium doped tin oxide (ITO)/PTAA substrates and was allowed to diffuse naturally to the other end of the substrate. The substrate was heated to 100 °C and then maintained between 110−120 °C for inducing nucleation and growth.[22] Yang et al. demonstrated a space-limited antisolvent vapor-assisted crystallization technique for the growth of all-inorganic $CsPbBr_3$ SCTF for photodetector application. In this approach, the bottom substrate was hydrophilic and the top surface was an octadecyltrichlorosilane-treated hydrophobic substrate. The precursor was filled in between the slit channel, and the entire setup was placed in a vessel containing acetonitrile antisolvent. The slow diffusion of the antisolvent results in nucleation and growth.[23] Pratheek et al. reported the growth of 10 μm-thick and 25 mm^2-sized MAPBr wafers using diffusion facilitated inverse temperature crystallization (DFITC) on ITO/PTAA substrates. They proposed that the hydrophobicity of the substrate plays a critical role in promoting homogeneous nucleation, resulting in large area SCTF.[24] Deng et al. reported the growth of centimeter-scale MAPBr SCTF using DFITC. They used a dimethyldimethoxysilane coated superhydrophobic glass substrate to grow MAPBr SCTF with an aspect ratio of 1000, i.e., 1 cm^2 area and 10 μm thick.[25−27]

Though the SC-PSCs are capable of producing highly efficient solar cells compared to their polycrystalline counterparts, growing large area single crystalline wafers is a challenging task. This is indicated by the fact that all the so-far reported SC-PSCs which returned PCEs consistently over 20% are all with miniscule sizes, with the grown crystal size (active area) restricted to a few millimeters square.[26,27] The photophysical characteristics of the large-area single crystalline perovskite wafers are another missing aspect of the available reports. In this context, here, we propose a graphite-based localized heating technique to grow large area MAPBr SCTF on a hydrophobic hole transporting PTAA coated ITO substrate (HTL), and also on a TiO_2 electron transporting layer (ETL) coated through a novel glancing angle deposition (GLAD) technique. Photoluminescence emission (PLE) and PL decay analyses are undertaken to investigate the charge transfer characteristics from the SCTF to the charge transfer layers (CTLs). In this work, we achieved, so far, large area (65 mm^2) SCTF wafers of MAPBr on different CTLs and show that the charge transport properties of the single crystalline wafers are much better than those of their polycrystalline counterpart.

2. EXPERIMENTAL PROCEDURE

2.1. Materials. Methylammonium bromide (MABr; >99.5%, Ossila), lead bromide (99.999%, Sigma), dimethylformamide (DMF; ≥99.9, Sigma), Poly[bis(4-phenyl)(2,4,6-trimethylphenyl)amine (PTAA; Mw = 56 kDa, Ossila), toluene (99%, Sigma), and ITO (Techinstro, 10 Ω/sq.) were purchased and used without any further purification. All the experiments were performed under ambient conditions (RH = 60−75% and RT = 30−34 °C).

2.2. Substrate Preparation. PTAA HTL: 5 × 5 cm^2 ITO substrates were cut and cleaned by the following procedure: the substrates were brushed using 2% Hellmanex solution in water, and sonicated in double distilled water, isopropyl alcohol, and acetone for 15 min each. The sonicated substrates were rinsed with isopropyl alcohol and dried at 100 °C inside a hot air oven followed by UV ozone (Holmarc Opto) treatment for 12 min. Two mg/mL solution of PTAA in toluene is prepared and spin coated on the ITO substrates at 3000 rpm for 30 s and annealed at 100 °C for 10 min.

GLAD of TiO_2 on ITO: TiO_2 powder was made into a pellet using hydraulic press and the pellets were sintered at 1200 °C for 4 h to obtain a compact TiO_2 pellet which is loaded to a graphite crucible in the e-beam evaporation chamber. The 5 × 5 cm^2 ITO substrate is cleaned by following the procedure mentioned earlier and then loaded to the substrate holder. The substrate holder is fixed at 80° angle for the GLAD. The 60 nm thick TiO_2 layer is deposited at 0.1 Å/s rate (e-beam: 4.5 kV and 30−40 mA) at a pressure of 1 × 10^{-5} mbar.

The properties of the as-deposited TiO_2 layer were investigated using UV−visible (UV−vis) transmittance and water contact angle (WCA) measurement. The transmittance of the ITO (Figure S1a) was found to be >95% while the TiO_2 coated ITO shows 80−85% transmittance in the visible region which is essential for solar cell application. The WCA measurement was performed to investigate the hydrophobic nature of the TiO_2 layer. The WCA of the TiO_2 coated ITO was found to be 99.3°, whereas the bare ITO was found to be 80.3° (Figure S1b). The thickness of the TiO_2 layer was measured using a stylus profilometer, and the average thickness was found to be ∼57 nm, which coincides with the thickness measured during the deposition.

2.3. Growth of SCTF. 1.5 M MAPBr precursor was prepared by mixing equimolar quantities of MABr and $PbBr_2$ in DMF and stirred vigorously overnight at room temperature. The homogeneous precursor was filtered using 0.2 μm PTFE filter moments before being dropped onto the substrate.

A localized heating setup using graphite rod [(purchased from Sunrise Enterprises, Maharashtra, India (thermal conductivity = 135 W m^{-1} K^{-1}))] and a Teflon block was developed. A graphite rod (2-in. length ×1 in. diameter) was inserted at the center of a 1-in. -thick Teflon block with the

https://doi.org/10.1021/acsomega.4c09505
ACS Omega 2025, 10, 10220−10229

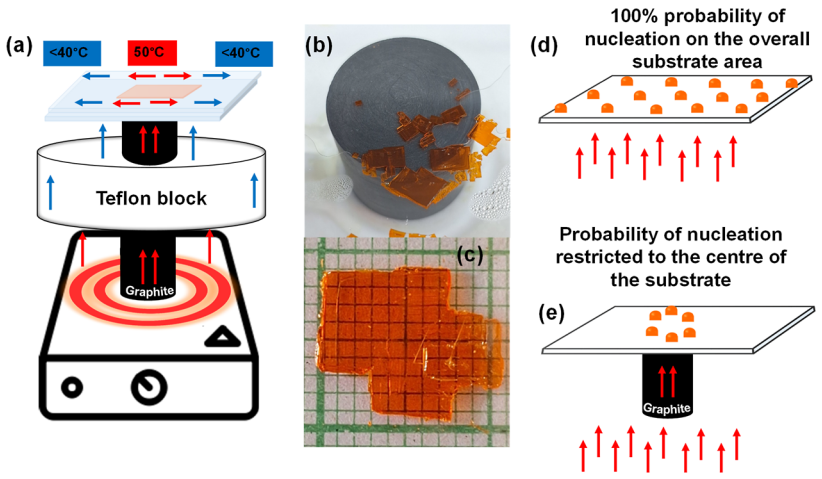

Figure 1. Graphite-based localized heating technique for large area MAPBr SCTF. (a) Schematic representation of the localized heating setup. (b) Real-time photograph of the localized heating setup with few small crystals at the graphite area. (c) The as-grown 65 mm^2 MAPBr SCTF. Schematic representation of the probability of nucleation for (d) direct hot plate heating and (e) localized heating.

graphite rod protruding from both the sides. One end of the graphite rod is placed on the hot plate which heats the graphite rod. Note that the Teflon block is not in direct contact with the hot plate. The cleaned substrates are sandwiched together and the MAPBr precursor is filled in the gap between the substrates. The sandwiched substrate is placed on top of the graphite rod and the temperature was gradually increased from room temperature (34 °C) to 50 °C at a heating rate of 5 °C/h. 2−3 crystals were observed only at the graphite region, while no crystal was observed in the remaining area of the substrate. This resulted in increasing the availability of more solution for larger crystal growth over a prolonged period. The growth was continued for 50 h, and the entire setup was kept undisturbed; SCTF as large as 65 mm^2 was finally obtained.

2.4. Growth of MAPBr Bulk Single Crystal. The bulk single crystals of MAPBr were successfully grown using an inverse temperature crystallization technique for comparison. 1.5 M of $PbBr_2$ and MAPBr were dissolved in 5 mL of DMF and stirred at room temperature overnight to obtain a homogeneous precursor solution. The solution was filtered using 0.2 μm PTFE syringe filter and immediately placed in an oil bath, and gradually heated to 50 °C at a rate of 5 °C/h. Orange colored MAPBr bulk single crystals of size 5 × 5 × 2 mm^3 were harvested after 12 h (Figure S2).

3. RESULTS AND DISCUSSION

3.1. Growth Mechanism of the Graphite-Based Localized Heating Technique. The growth of SCTF via DFITC is different from conventional bulk crystal growth. In the case of the bulk growth, the ideal growth temperature for 1.5 M precursor solution of MAPBr was found to be 50 °C, and the system needs to be maintained at this temperature throughout the growth period. This is comparatively an easy task and does not raise any concern since the probable nucleation site is constrained only to the bottom of the growth vessel and the crystal is free to grow in all directions.[28] However, it is not the same for the case of DFITC, since every point throughout the substrate is a feasible site for nucleation, and the constant supply of heat results in a polycrystalline film. Thus, maintaining the appropriate temperature during the course of the growth process is not an easy task. The next concern regarding the DFITC technique is the very limited volume of the precursor (a few microliters) available for the crystal to grow into a larger size. During DFITC, the precursor is sandwiched between two substrates and the sandwiched substrate is heated to induce supersaturation of the precursor followed by nucleation through ITC.[29] However, heating the entire substrate results in nucleation all over the substrate, followed by the growth of numerous small crystals (Figure S3).[30] The problem arises when these small crystals consume the solutes present in the precursor, resulting in a rapid depletion of the solutes which restricts the crystals from growing into larger sizes. Thus, precise control over the growth temperature on the substrate is crucial for controlling the nucleation.

To overcome this challenge, we developed a localized heating technique to manipulate the heat transferred to the substrate and thereby restrict the probability of nucleation within a specific area of the substrate. The localized heating setup is fairly simple where, instead of directly heating the glass/ITO/PTAA substrate (5 × 5 cm^2) on a hot plate, the heat from the hot plate is transferred to the substrate through a graphite rod of 1-in. diameter and 2-in. length. The graphite rod is inserted at the center of a 1 in. thick Teflon block with the graphite rod protruding from both the sides. The Teflon block shields the heat radiated from the hot plate to the substrate, and the heat from the hot plate can be transferred to the substrate only through the graphite rod (Figure 1a). Thus, the path of heat transfer from the source to the substrate is via hot plate → graphite → substrate. This results in a localized heating at the center of the substrate, which is tuned to the desired growth temperature (50 °C) with the temperature reducing gradually as we move from the center to the edge of the substrate (Figure S4). This results in nucleation only at the center of the substrate, and eventually, 2−3 small crystals were initially observed (Figure 1b). These small crystals then grow to larger sizes using the precursor available outside the graphite area (which is at a temperature lower than the crystallization temperature). This method consistently returned large area MAPBr SCTF wafers of up to a 65 mm^2 size (Figure 1c). The nucleation kinetics involved in this localized heating is schematically explained in Figure 1d,e. When the substrate is heated on a hot plate, the hot surface is directly in contact with the entire substrate heating it evenly throughout. The uniform

https://doi.org/10.1021/acsomega.4c09505
ACS Omega 2025, 10, 10220−10229

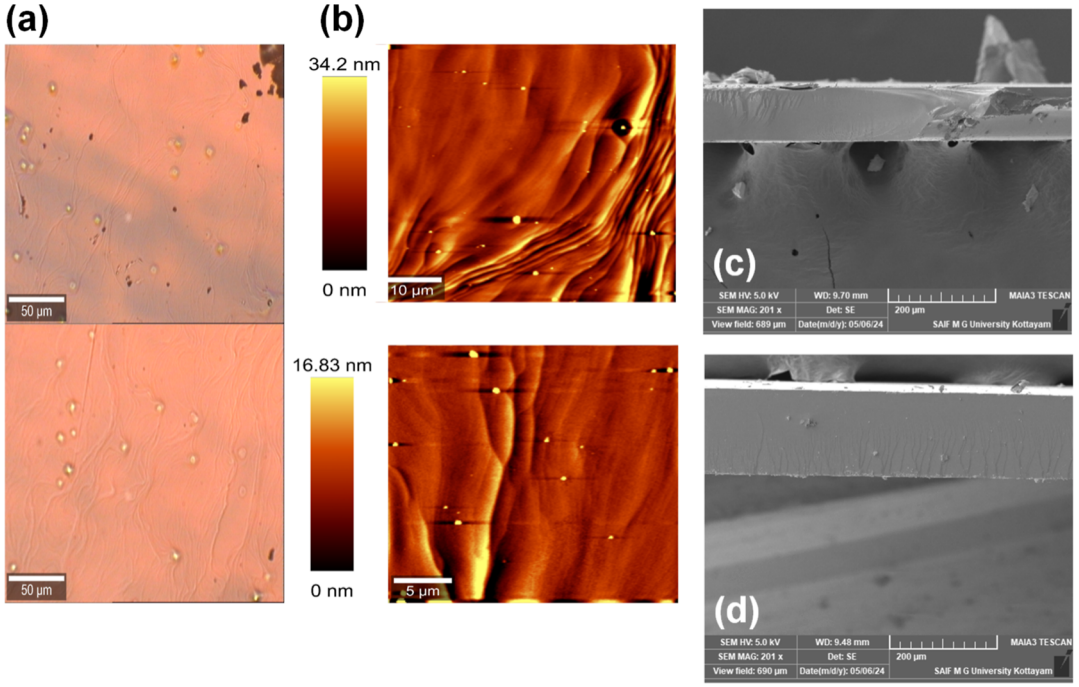

Figure 2. (a) Optical microscope image at two different spots on the SCTF showing similar features. (b) AFM images of the as-grown large-area SCTF wafer at different scan area (20 × 20 and 50 × 50 μm^2). Cross-sectional SEM micrographs of MAPBr SCTF grown (c) without seed and (d) with seed.

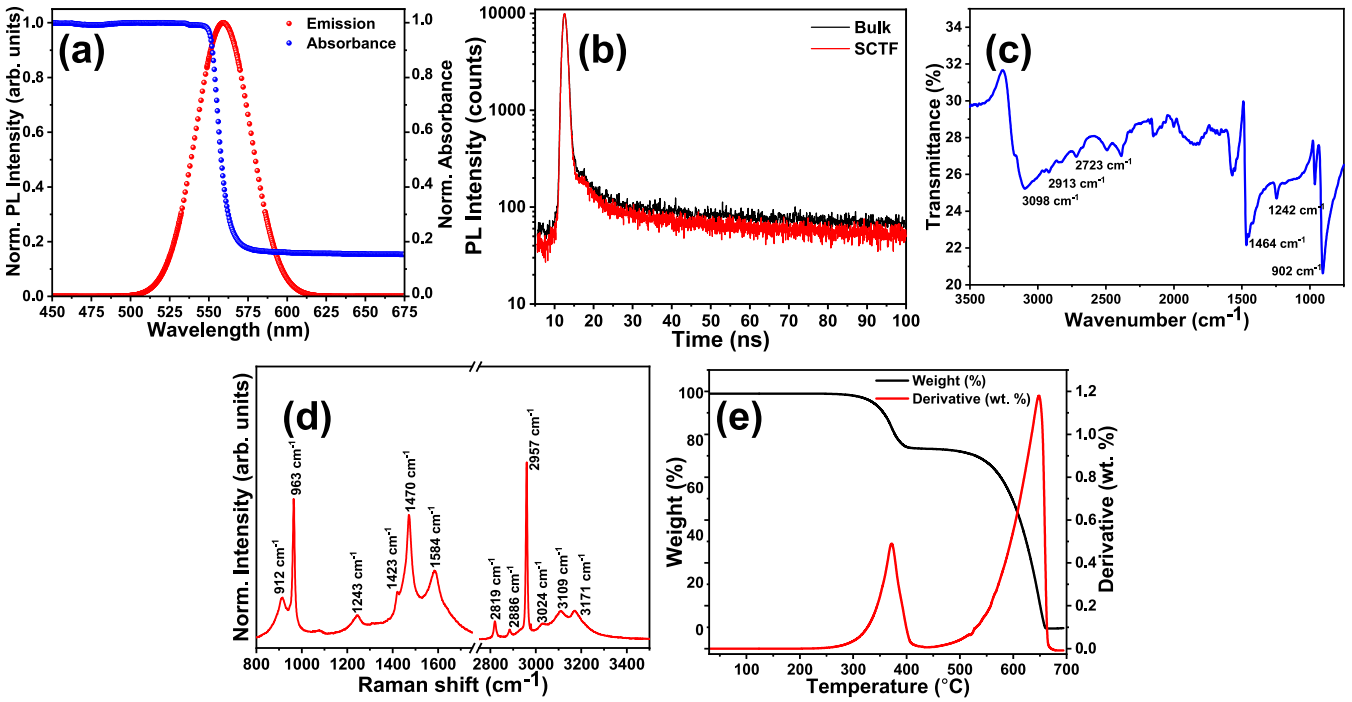

Figure 3. Characterization of the as-grown MAPBr SCTF. (a) UV−Vis absorbance and steady-state PLE curves. (b) PL decay lifetime curve of bulk and SCTF MAPBr. (c) FTIR and (d) Raman spectra exhibiting all the major peaks corresponding to the as-grown MAPBr SCTF. (e) TG-DTA curve of MAPBr SCTF indicating thermal stability up to 200 °C.

heating of the substrate indicates that the probability of nucleation is 100% throughout the substrate area (Figure 1d). However, when the substrate is locally heated from the center, the heat radiated to the area outside the central area is blocked using a heat insulator, causing the probability of nucleation to be restricted within the area in contact with the heat source (Figure 1e). This makes the precursor in the remaining substrate area to be well below the growth temperature (50 °C).

3.2. Characterization of the As-Grown Large Area SCTF. The as-grown 65 mm^2 SCTF was analyzed using various structural, optical, thermal, and morphological techniques to confirm it as a phase-pure single crystal and not a group of small crystals merged together. Unless otherwise mentioned,

https://doi.org/10.1021/acsomega.4c09505
ACS Omega 2025, 10, 10220−10229

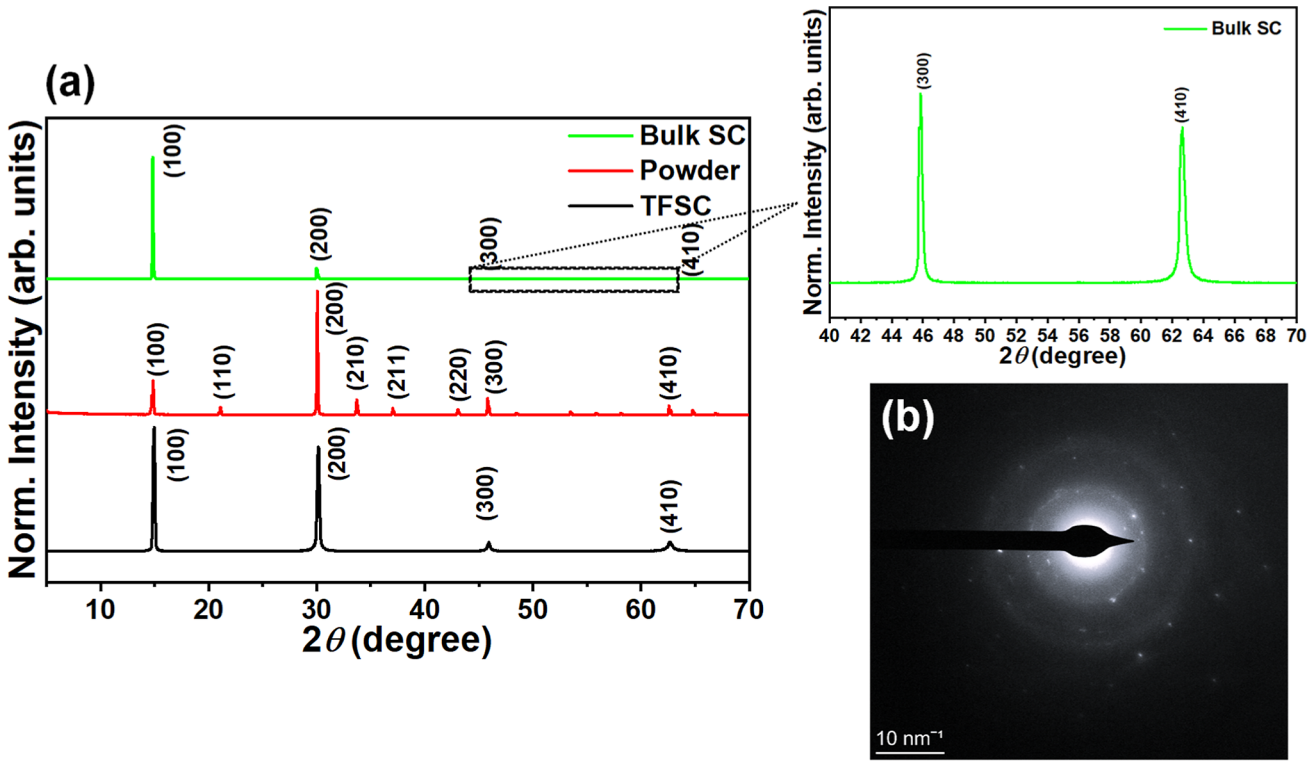

Figure 4. (a) PXRD patterns of MAPBr SCTF, polycrystalline powder, and bulk single crystal. (b) SAED patter of the MAPBr SCTF.

all the analyses were performed on the as-grown large area SCTF wafer. The optical microscope image (Figure 2a) depicts a smooth, planar surface with pinhole-like features and wave-like patterns on the SCTF surface. The atomic force microscopy (AFM) topography imaging was employed to understand the pinhole like structures. It was observed that (Figure 2b) these are not pinholes and can be attributed to some dust particles sticking on the SCTF surface. The wave-like patterns observed on the surface of the SCTF are attributed to the uneven surface of the PTAA layer. The average surface roughness of the SCTF is measured to be R_a = 4.37 ± 0.01 nm (for 50 × 50 μm^2 scan area). This highly smooth surface will be beneficial for reducing the interfacial charge recombination in the heterojunction PSC.[31,32] Additionally, the wave-like pattern on the crystal surface implies that the surface morphology of the substrate directly impacts the surface morphology of the SCTF wafer, and hence it is desired to deposit a smooth and planar CTL. The wafers were grown in two ways to experiment the impact of a seed crystal: In one case, continuous DFITC-based confined growth is followed. In the second case, one seed initially formed was taken out and kept in between two new substrates and allowed to grow larger by adding fresh precursor. This was done to understand the impact of using a single seed on the thickness of the as-grown wafer compared to direct nucleation. Utilizing a small seed crystal for growing bulk single crystals is a well-known technique to obtain faster supersaturation and controlled crystal orientation. Manipulating the SCTF thickness can assist in promoting SCTF wafers for a wide range of applications. Hence, this comparison was made to also provide additional insights into the crystal growth process, and the thicknesses of the SCTFs were compared to depict the impact of using a seed. The cross-sectional SEM was employed to measure the SCTF thickness. In order to eliminate any discrepancy due to the substrate during the thickness measurement, a small piece of the SCTF was broken to obtain a free-standing thin crystal and was loaded into the SEM chamber for cross-sectional imaging. The cross-sectional SEM micrographs (Figure 2c,d) clearly depict the increase in the thickness of the SCTF at the same magnification of 201×. It is observed that SCTF grown with direct nucleation and continuous growth has a thickness of ∼97.09 ± 1.3 μm (Figure 2c), while SCTF grown using a small seed crystal shows a higher thickness of ∼159.18 ± 1.1 μm (Figure 2d). The higher thickness might be due to the increased distance between the two substrates due to the presence of seed.

The optical and photophysical properties of the SCTF wafers grown on ITO/PTAA substrate were investigated using UV−Vis absorption, steady-state PLE, and PL decay analyses. The UV−Vis absorption spectrum of SCTF given in Figure 3a shows the typical absorption characteristic of MAPBr with the absorption edge around ∼555 nm. The corresponding PLE spectrum (λ_{ex} = 395 nm) shows the characteristic emission peak at ∼565 nm which corresponds to a bandgap of 2.2 eV. The overlaid absorption and emission spectra depict the well-known band-edge emission characteristic of the MAPBr perovskite (Figure 3a).[33] The PL decay curves were compared with the bulk single crystal to demonstrate a distinction between the SCTF and the bulk crystal. The PL decay lifetime of the SCTF wafer was monitored at 565 nm emission (λ_{ex} = 395 nm), and the same was compared with the bulk MAPBr single crystal. The PL decay curves of the bulk and SCTF wafer almost overlap each other, indicating similar lifetime characteristics (Figure 3b). The decay constants of the bulk single crystal were found to be τ_1 = 3.16 ± 0.84 ns, τ_2 = 13.34 ± 0.49 ns, and τ_3 = 57.17 ± 0.37 ns while that of the SCTF was found to be τ_1 = 3.9 ± 0.44 ns, τ_2 = 14.01 ± 0.32 ns, and τ_3 = 58.57 ± 0.11 ns. This indicates that reducing the thickness of the bulk

https://doi.org/10.1021/acsomega.4c09505
ACS Omega 2025, 10, 10220−10229

crystal does not impact the charge carrier lifetime characteristic. This is a very critical observation for application-oriented device fabrication, as bulk single crystal-like carrier lifetime has been achieved here in the case of the SCTF.

The molecular structure of MAPBr was analyzed by using FTIR (Figure 3c) and Raman (Figure 3d) spectroscopy. The FTIR spectra shows the presence of the characteristic vibrations of MAPBr with all the major vibrations. The 900−3500 cm^{-1} region in the Raman spectrum (λ_{ex} = 532 nm) of MAPBr (Figure 3d) corresponds to the dominant vibration of the MA^+ cation. The strong peak at 2957 cm^{-1} and a weak peak at 1423 cm^{-1} correspond to the asymmetric stretching of CH_3 and the 963 cm^{-1} peak corresponds to the CH_3 deformation. All the major peaks observed can be assigned with the strong vibrations of the MA^+ ($CH_3NH_3^+$) cation. The presence of all the characteristic peaks and the absence any foreign peak in the as-grown MAPBr SCTF indicate that there are no residual impurities in the as-grown SCTF. The thermal decomposition characteristic of the MAPBr SCTF was analyzed using thermogravimetry-differential thermal analysis (TG-DTA). The MAPBr SCTF wafer was crushed into a coarse powder before performing the TG analysis. The TG-DTA curve of the MAPBr SCTF (Figure 3e) shows ∼20% weight loss at ∼360 °C indicating the decomposition of the hydrobromic acid (HBr) and other organic elements, and 100% weight loss was observed at ∼640 °C. The analysis reveals that the compound is thermally stable up to ∼200 °C and significant thermal decomposition is observed only above ∼300 °C.

The crystallographic and structural properties of the as-grown SCTF were investigated by using single crystal and powder X-ray diffraction (XRD) analyses. The powder XRD experiment was performed on the as-grown MAPBr SCTF, polycrystalline powder, and bulk single crystal. The comparison of the results facilitates to understand the distinction in the crystalline properties of the SCTF (this work) and the polycrystalline and single crystal reference samples. The XRD pattern (Figure 4a) for the powdered SCTF presents the peaks corresponding to the polycrystalline MAPBr, while that of the SCTF and the bulk single crystal show only the major peaks corresponding to the (100), (200), (300), and (410) planes of the cubic phase MAPBr. It can be noted that all the major diffraction peaks corresponding to the cubic ($Pm3/m$) phase of MAPBr are present for all three forms of the crystal. The similar XRD patterns for the bulk crystal and the SCTF again highlight the crystalline quality of the SCTF. The presence of sharp, high intensity peaks and absence of any other impurity/secondary peaks for the SCTF indicate that the as-grown MAPBr SCTF is phase-pure and free of any residual impurities. The single crystal XRD analysis revealed that the as-grown MAPBr SCTF wafer belongs to the $Pm3/m$ space group corresponding to the cubic phase with the unit cell parameters: $a = b = c$ = 5.94 Å, $\alpha = \beta = \gamma = 90°$ and unit cell volume of 210 $Å^3$, which match with the existing COD database (Card no. 1545320). The selected area electron diffraction (SAED) image (Figure 4b) was obtained from a small piece (1−2 mm size) cleaved from the edge of the SCTF. The SAED image depicts a square-like pattern of the diffraction spots corresponding to the (100), (200), and (300) planes of the cubic phase MAPBr crystal. These crystallographic analyses further denote that the as-grown large area SCTF is an actual single crystal and not a group of small crystals merged together. The results also coincide with the observations made from the FTIR and Raman analyses, suggesting that large area SCTFs of phase-pure MAPBr can be successfully grown using the localized heating-based DFITC technique under ambient conditions.

The crystallinity of the perovskite absorber layer plays a major role in the optoelectronic and structural stability of the hybrid lead halide perovskite thin films. Thin films with high degree of crystallinity reduce the photogenerated charge carrier recombination at the defects (i.e., grain boundaries) in a polycrystalline thin film. The superiority of the SCTF compared to the polycrystalline film remains on the fact that the SCTF is made of a single grain, which eliminates the recombination losses. Thus, the crystallinity of the as-grown large-area SCTF was determined by calculating the crystallinity index (CI) from the XRD data and compared with those of the bulk single crystal and polycrystalline forms of MAPBr. The CI is given by the following relation

$$\mathrm{CI} = \frac{\text{Area of crystalline peaks}}{\text{Total area of the peaks}} \times 100(\%)$$

which is the ratio of the area of the crystalline peaks to the total area of the peaks (crystalline + amorphous). The XRD pattern in Figure 4a was used for the CI calculation, where the CI of bulk single crystal was found to be 97.74 ± 0.47% while that of the polycrystalline MAPBr was found to be 69.80 ± 0.60%. The lower CI for the polycrystalline MAPBr is a direct implication of the multiple number of crystals present in the polycrystalline phase, which increases the amorphous nature. The CI value of close to 100% for the bulk single crystal indicates the high degree of crystallinity, which is ideal for any application. The CI of the SCTF was found to be 92.60 ± 0.11%, which is similar to the CI value of the bulk single crystal. The almost-comparable crystallinity indices of the bulk single crystal and the SCTF correspond to the observations made from the optical properties of the SCTF (Figure 3a,b), which delineate the fact that bulk single crystal-like properties have been achieved for the SCTF which is beneficial for device applications. The CI values also emphasize that the localized heating technique does not have any major impact on reducing the crystallinity of the large area SCTF.

3.3. Charge Transfer Characteristic in SCTF. The charge transfer characteristic in a polycrystalline thin film based PSCs is a well-established concept.[34−36] Although there are several reports on the growth of SCTF, to the best of our knowledge, there are no reports available on the charge transfer properties of the SCTFs grown on top of different ETL and HTL. It is important to analyze the kinetics of the photogenerated charge carriers in the SCTF, since the knowledge of the charge transfer between the SCTF and CTL is crucial in fabricating large area SCTF based devices. Hence, an attempt has been made here to grow MAPBr SCTFs on ITO substrates with different buffer layers, viz. glass/ITO, glass/ITO/PTAA (HTL), and glass/ITO/TiO_2 (ETL) and their steady-state PLE and PL decay lifetime characteristics were analyzed. Unlike the earlier sections, where the characteristics of the SCTF were compared with the bulk single crystal or polycrystalline MAPBr, in this section, we have kept the MAPBr SCTF grown on glass substrate (non-conducting) as the standard reference, the PLE and PL decay characteristics of the MAPBr SCTFs grown on different conducting substrates (ITO, PTAA, and TiO_2) are compared. We propose an experiment analogous to the conventional PL

https://doi.org/10.1021/acsomega.4c09505
ACS Omega 2025, 10, 10220−10229

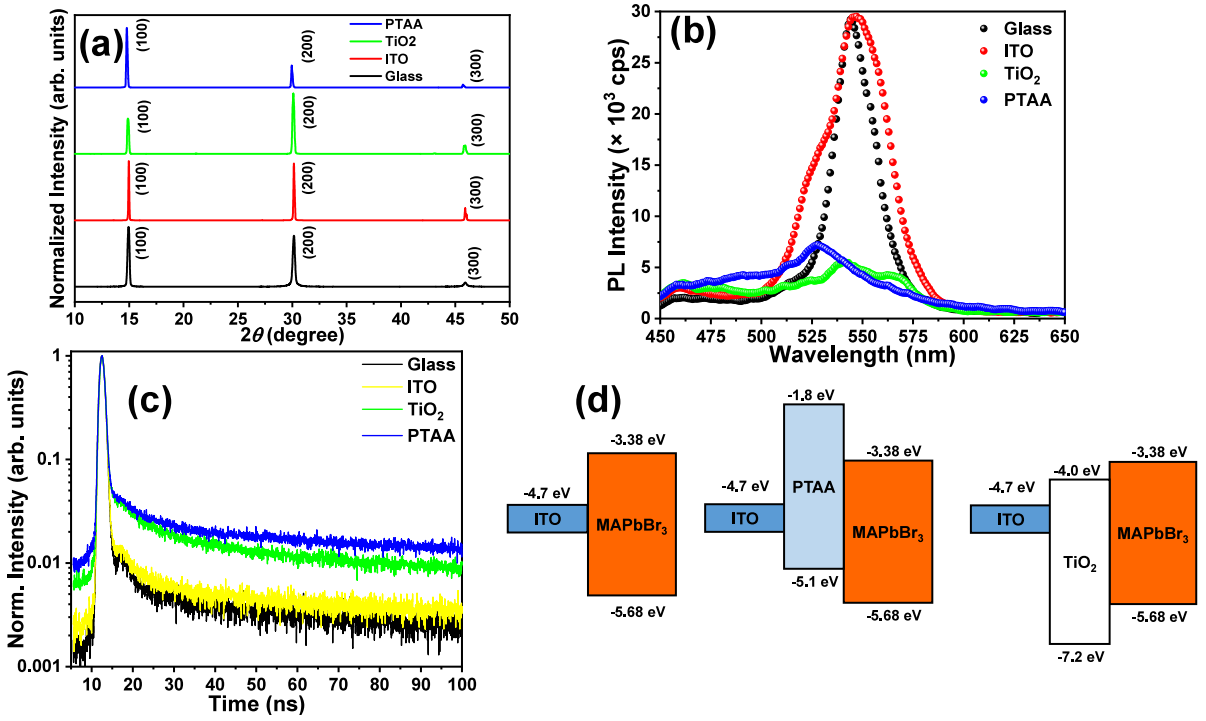

Figure 5. (a) XRD, (b) PLE, and (c) PL decay curves of MAPBr SCTF grown on various substrates (the SCTFs were illuminated from the crystal side). (d) Band alignment diagram for MAPBr SCTF grown on various substrates.

quenching analysis for polycrystalline perovskite thin films.[37] The PL quenching analysis is a conventional PL measurement performed on a thin film fabricated with and without a CTL (exciton quenching layer) on top the polycrystalline film.[38−40] In this work, we follow a similar approach, where instead of depositing the CTL on top of the SCTF, we deposit the hydrophobic CTL first, and the SCTFs were grown on top of the CTLs. This allows us to understand the charge transport from the SCTF to the CTL, i.e., any change in the PL characteristics can be directly ascribed to the photogenerated charge carriers being injected into the CTL. Additionally, we have performed the experiment on both HTL/perovskite and ETL/perovskite configurations, which is essential for device fabrication in p−i−n and n-i-p configurations. We initially performed XRD analysis on the SCTFs grown on top of different CTLs in order to demonstrate that there is no change in the SCTF crystallinity due to the CTLs. The XRD peaks for all the crystals grown on different substrates exhibited identical patterns corresponding to the cubic phase of MAPBr (Figure 5a). The sharp peaks indicate superior crystallinity of the SCTF which is comparable to that of the pristine sample presented in Figure 4. It is noteworthy to mention that the steady-state PLE and decay lifetime analyses were performed by placing the SCTF at the center of the sample holder with the SCTF illuminated from the crystal side.

The steady-state PLE (λ_{ex} = 395 nm) curve in Figure 5b presents the characteristic emission of MAPBr for the glass substrate. The sharp, high intensity peak signifies the pristine quality of the SCTF enabling the emission of the majority of the photogenerated charge carriers due to the lack of any hindrance from the substrate. The MAPBr SCTF grown on a glass/ITO substrate shows a similar PLE curve but with a larger fwhm, which can be due to the charge recombination at the ITO/perovskite interface. However, both curves trace a similar characteristic which can be ascribed to the typical emission of MAPBr. The PLE curves of the SCTFs grown on glass/ITO/PTAA and glass/ITO/TiO_2 substrates demonstrate a drastic drop in the PLE intensity, which indicates the exciton quenching behavior, denoting that the photogenerated charge carriers are injected into the CTLs. We observe a similar phenomenon which has been proposed for several other hybrid lead halide perovskites with the quenching layer on top of the polycrystalline thin film.[41−43]

The PL decay analysis was performed following the exact procedure employed for the PLE measurement. The samples were excited at 390 nm, and the PL decay was observed at 565 nm. The overlaid PL decay spectra for all the samples (Figure 5c) indicate that the SCTF grown on bare glass substrate exhibits the longest lifetime (Table 1). This can be attributed to the lower exciton recombination within the SCTF due to the lack of grain boundaries and interfacial recombination. The SCTF grown on glass/ITO substrate also presented a similar decay characteristic, with a slight decrease in the decay lifetime, while the lifetimes of the SCTFs grown on TiO_2 and PTAA substrates were decreased significantly. The slight decrease in the decay lifetime for the ITO substrate can be due to the charge accumulation at the ITO/perovskite interface, which results in recombination. The shorter lifetime of the SCTF on TiO_2 and PTAA can be ascribed to the injection of the photogenerated charge carriers into their respective CTLs (i.e.,

Table 1. Lifetime Parameters Obtained from the Tri-exponential Fitting of the PL Decay Curves

substrate	τ_1 (ns)	τ_2 (ns)	τ_3 (ns)
glass	4.77 ± 0.18	19.19 ± 0.16	68.28 ± 0.29
glass/ITO	4.61 ± 0.19	12.05 ± 0.23	55.63 ± 0.46
glass/ITO/PTAA	3.15 ± 0.33	4.57 ± 0.71	39.68 ± 0.13
glass/ITO/TiO_2	3.32 ± 0.07	5.79 ± 0.18	45.74 ± 0.23

https://doi.org/10.1021/acsomega.4c09505
ACS Omega 2025, 10, 10220−10229

Table 2. Comparison of the Absorption Band Edge, PLE, and PL Decay Lifetime of the Previously Reported MAPBr Polycrystalline Film With Our SCTF

film type	substrate	Abs. band edge (nm)	PLE peak position (nm)	PL decay lifetime, τ_3 (ns)	ref
polycrystalline film	glass	521	530 (λ_{ex} = 405 nm)		44
polycrystalline film	ITO	∼530	536 (λ_{ex} = 405 nm)	51	45
polycrystalline film	glass		∼530		46
polycrystalline film	FTO	540−550			47
SCTF	glass	555	565 (λ_{ex} = 395 nm)	68.28 ± 0.29	this work
SCTF	ITO	555	565 (λ_{ex} = 395 nm)	55.63 ± 0.46	this work

electrons into TiO_2 and holes into PTAA). This, also, results in an accelerated decay due to the charge recombination at the CTL/perovskite interface. The decrease in the fast decay constant from τ_1 = 4.77 ± 0.18 ns for glass to τ_1 = 3.32 ± 0.07 ns for TiO_2 and τ_1 = 3.15 ± 0.33 ns PTAA is a clear evidence of the charge injection into the respective CTLs, which can be correlated with the decrease in the PLE intensity (Figure 5b). The interpretation of the decay curves with the band alignment diagram (Figure 5d) indicates the free flow of both electrons and holes into their respective CTLs, thus reducing the fast decay component (τ_1) due to the immediate injection of charge carriers. These results emphasize the PL quenching behavior of the SCTFs grown on different substrates grown using localized heating technique and make them ideal for various optoelectronic and photovoltaic applications.

The optical properties (absorption band edge, PLE peak position, and PL decay lifetime) of the MAPBr SCTF are compared with the previously reported polycrystalline MAPBr thin films grown on different substrates (Table 2). The polycrystalline films deposited via spin coating and vacuum deposition exhibit an absorption edge in the range of 520−550 nm and PLE around ∼530 nm, while our SCTF shows an absorption edge at 555 nm and PLE at 565 nm. The comparison enables us to understand the significance of the SCTF, especially the below bandgap transition due to the reduced defects, resulting in a redshift of the absorption edge and the emission peak. The PL lifetime is also increased from 55.63 ± 0.46 ns for the SCTF on ITO substrate, while the polycrystalline film exhibits a decay lifetime of 51 ns on ITO substrate. The lower PL decay lifetime for the polycrystalline thin film can be attributed to the charge carrier recombination at the grain boundaries, and the SCTFs show enhanced lifetime due to the single crystalline nature and the absence of grain boundaries.

In summary, 65 mm^2-sized MAPBr SCTF wafer was grown using a graphite based localized heating technique, and the SCTF quality was analyzed using various characterization techniques. The PLE quenching and faster PL decay for the MAPBr SCTF grown on PTAA and TiO_2 substrates indicate the swift injection of the photogenerated charge carriers into the respective CTLs which is crucial for device fabrication.

Although the proposed graphite-based localized heating technique can produce large-size SCTF, the size of the crystal relies on the amount of solute available for continuous crystallization. This is an obvious limitation in the solution based crystal growth technique, which can be addressed by adapting the following modifications: (i) large area substrates can be employed for SCTF wafer growth. In this work, we have sandwiched two 5 × 5 cm^2 ITO coated glass substrates, which accommodated ∼200 μL of the fresh precursor resulting in an SCTF size of 65 mm^2. Increasing the substrate area, e.g., 10 × 10 cm^2, will result in the availability of more precursor which can facilitate the continuous growth of the SCTFs with much larger lateral dimensions. (ii) Continuous supply of fresh precursor from an external reservoir can be employed. (iii) Intermittent growth can be adapted by following consecutive cycles of heating and cooling. Once the entire solute is consumed, the setup can be cooled to the room temperature and fresh precursor can be added to the substrate and heated again to continue the growth process.

4. CONCLUSIONS

A graphite-based localized heating technique for growing comparatively large area (up to ∼65 mm^2 size) $MAPbBr_3$ SCTFs under ambient conditions was developed. It was observed that the localized heating can induce supersaturation at a particular area on the substrate. The graphite-based localized heating setup resulted in the considerable reduction in the number of seeds formed and these are largely confined only to the graphite heating area, and no nucleation was observed at the remaining area of the substrate. The structural, optical, morphological, and thermal analyses revealed that the as-grown MAPBr SCTF is phase-pure without any residual impurities. The AFM results suggest that the surface topography of the substrate plays a critical role in the topography of the SCTF with a roughness of R_a = 4.37 ± 0.01 nm. The PL decay lifetimes of both the bulk single crystal and SCTF were found to be similar, which implies that the reduced crystal thickness does not impact the charge carrier lifetime. The absence of any secondary peaks in the XRD pattern indicated that the as-grown SCTF is an actual single crystal and not a group of small crystals merged together. The PLE curves exhibited a significant quenching of the emission intensity for the SCTFs grown on TiO_2 and PTAA substrates, which can be ascribed to the exciton quenching effect. The abrupt decrease in the fast decay component of the SCTF from τ_1 = 4.77 ± 0.18 ns for glass to τ_1 = 3.32 ± 0.07 ns for TiO_2 and τ_1 = 3.15 ± 0.33 ns PTAA evidences the injection of charge carriers into the respective CTL and the decreased overall lifetime is ascribed to the interfacial recombination of the charges accumulated at the CTL/perovskite interface.

■ ASSOCIATED CONTENT

Data Availability Statement

The raw data underlying this study are not publicly available since it forms a part of an ongoing research project.

Supporting Information

The Supporting Information is available free of charge at https://pubs.acs.org/doi/10.1021/acsomega.4c09505.

UV−Vis transmittance spectrum and water contact angle of ITO and TiO_2 coated ITO substrates; photographs of the as-grown MAPBr bulk single crystal and cluster of

https://doi.org/10.1021/acsomega.4c09505
ACS Omega 2025, 10, 10220−10229

tiny crystals due to heterogeneous nucleation; and temperature profile (PDF)

AUTHOR INFORMATION

Corresponding Authors

Linda Cattin − *Institut des Materiaux de Nantes Jean Rouxel (IMN), CNRS, UMR 6502, Nantes Université, Nantes 44322, France;* orcid.org/0000-0002-8222-5929; Email: Linda.Cattin-Guenadez@univ-nantes.fr

Predeep Padmanabhan − *School of Nanoscience and Nanotechnology, Mahatma Gandhi University, Kottayam 686560 Kerala, India*; Email: predeep@mgu.ac.in

Authors

Mano Balaji Gandhi − *School of Nanoscience and Nanotechnology, Mahatma Gandhi University, Kottayam 686560 Kerala, India; Institut des Materiaux de Nantes Jean Rouxel (IMN), CNRS, UMR 6502, Nantes Université, Nantes 44322, France;* orcid.org/0000-0003-0135-9675

Aiswarya Mohan − *Department of Physics, National Institute of Technology Calicut, Calicut 673603 Kerala, India*

Sreekala Meyyarappallil Sadasivan − *School of Nanoscience and Nanotechnology, Mahatma Gandhi University, Kottayam 686560 Kerala, India;* orcid.org/0000-0002-9357-0947

Sabu Thomas − *School of Nanoscience and Nanotechnology, Mahatma Gandhi University, Kottayam 686560 Kerala, India;* orcid.org/0000-0003-4726-5746

Angappane Subramanian − *Centre for Nano and Soft Matter Sciences (CeNS), Bangalore 562162 Karnataka, India;* orcid.org/0000-0001-8475-0404

Jean Christian Bernède − *2 MOLTECH-Anjou, CNRS, UMR 6200, Nantes Université, Nantes 44322, France;* orcid.org/0000-0002-1457-1117

Guy Louarn − *Institut des Materiaux de Nantes Jean Rouxel (IMN), CNRS, UMR 6502, Nantes Université, Nantes 44322, France;* orcid.org/0000-0003-0683-7381

Complete contact information is available at: https://pubs.acs.org/10.1021/acsomega.4c09505

Notes

The authors declare no competing financial interest.

ACKNOWLEDGMENTS

The authors thankfully acknowledge the Indo−French Centre for the Promotion of Advanced Research (IFCPAR/CEFIPRA) for the financial support under project no. 6708-1. The authors thank the Department of Science and Technology−Sophisticated Analytical Instrumentation Facility (DST−SAIF) at the Mahatma Gandhi University, Kottayam, for the SEM, AFM, Raman, and PL characterization facilities. The authors are grateful to Prof. Moorthy Babu Sridharan and Sai Prasanna Meenakshisundaram, Crystal Growth Centre, Anna University, Chennai, for their support with the SAED analysis.

REFERENCES

(1) Sherkar, T. S.; Momblona, C.; Gil-Escrig, L.; Ávila, J.; Sessolo, M.; Bolink, H. J.; Koster, L. J. A. Recombination in Perovskite Solar Cells: Significance of Grain Boundaries, Interface Traps, and Defect Ions. *ACS Energy Lett.* **2017**, *2* (5), 1214−1222.

(2) Jia, P.; Qin, L.; Zhao, D.; Tang, Y.; Song, B.; Guo, J.; Li, X.; Li, L.; Cui, Q.; Hu, Y.; et al. The Trapped Charges at Grain Boundaries in Perovskite Solar Cells. *Adv. Funct. Mater.* **2021**, *31* (49), 2107125.

(3) Castro-Méndez, A.-F.; Hidalgo, J.; Correa-Baena, J.-P. The Role of Grain Boundaries in Perovskite Solar Cells. *Adv. Energy Mater.* **2019**, *9* (38), 1901489.

(4) Shockley, W.; Queisser, H. J. Detailed Balance Limit of Efficiency of p-n Junction Solar Cells. *J. Appl. Phys.* **1961**, *32* (3), 510−519.

(5) Lee, Y. H. Beyond the Shockley-Queisser limit: Exploring new frontiers in solar energy harvest. *Science* **2024**, *383* (6686), No. eado4308.

(6) Rong, S.-S.; Faheem, M. B.; Li, Y.-B. Perovskite single crystals: Synthesis, properties, and applications. *J. Electron. Sci. Technol.* **2021**, *19* (2), 100081.

(7) Cheng, X.; Yang, S.; Cao, B.; Tao, X.; Chen, Z. Single Crystal Perovskite Solar Cells: Development and Perspectives. *Adv. Funct. Mater.* **2020**, *30* (4), 1905021.

(8) Chen, Z.; Turedi, B.; Alsalloum, A. Y.; Yang, C.; Zheng, X.; Gereige, I.; AlSaggaf, A.; Mohammed, O. F.; Bakr, O. M. Single-Crystal MAPbI3 Perovskite Solar Cells Exceeding 21% Power Conversion Efficiency. *ACS Energy Lett.* **2019**, *4* (6), 1258−1259.

(9) Alsalloum, A. Y.; Turedi, B.; Zheng, X.; Mitra, S.; Zhumekenov, A. A.; Lee, K. J.; Maity, P.; Gereige, I.; AlSaggaf, A.; Roqan, I. S.; et al. Low-Temperature Crystallization Enables 21.9% Efficient Single-Crystal MAPbI3 Inverted Perovskite Solar Cells. *ACS Energy Lett.* **2020**, *5* (2), 657−662.

(10) Alsalloum, A. Y.; Turedi, B.; Almasabi, K.; Zheng, X.; Naphade, R.; Stranks, S. D.; Mohammed, O. F.; Bakr, O. M. 22.8%-Efficient single-crystal mixed-cation inverted perovskite solar cells with a near-optimal bandgap. *Energy Environ. Sci.* **2021**, *14* (4), 2263−2268.

(11) Almasabi, K.; Zheng, X.; Turedi, B.; Alsalloum, A. Y.; Lintangpradipto, M. N.; Yin, J.; Gutiérrez-Arzaluz, L.; Kotsovos, K.; Jamal, A.; Gereige, I.; et al. Hole-Transporting Self-Assembled Monolayer Enables Efficient Single-Crystal Perovskite Solar Cells with Enhanced Stability. *ACS Energy Lett.* **2023**, *8* (2), 950−956.

(12) Lintangpradipto, M. N.; Zhu, H.; Shao, B.; Mir, W. J.; Gutiérrez-Arzaluz, L.; Turedi, B.; Abulikemu, M.; Mohammed, O. F.; Bakr, O. M. Single-Crystal Methylammonium-Free Perovskite Solar Cells with Efficiencies Exceeding 24% and High Thermal Stability. *ACS Energy Lett.* **2023**, *8* (11), 4915−4922.

(13) Tsvetkov, N.; Koo, D.; Kim, D.; Park, H.; Min, H. Advances in single-crystal perovskite solar cells: From materials to performance. *Nano Energy* **2024**, *130*, 110069.

(14) Li, C.; Chen, C. Single-Crystal Perovskite for Solar Cell Applications. *Small* **2024**, *20* (48), 2402759.

(15) Liu, N.; Li, N.; Jiang, C.; Han, D.; Dai, J.; Niu, Y.; Dou, Y.; Chen, S.; Chen, Y.; Chen, Z.; et al. Recycling Single-Crystal Perovskite Solar Cells With Improved Efficiency and Stability. *Adv. Funct. Mater.* **2024**, *34* (52), 2410631.

(16) McCleese, C. L.; Brennan, M. C.; Episcopo, N.; Sun, L.; Hong, N.; Ramana, C. V.; Grusenmeyer, T. A.; Stevenson, P. R. Optical Dispersion Data Analysis of Single-Crystal $CH_3NH_3PbBr_3$ for Optimized Perovskite Solar Cell Active Layer Absorptance. *Adv. Photonics Res.* **2024**, *5* (10), 2400019.

(17) Li, D.; Li, N.; Zou, C.; Zhong, Y.; Qu, Y.; Yang, S.; Wang, L.; Chen, Y.; Cheng, X.; Tao, X.; et al. Efficient and Highly Stable Lateral Perovskite Single-Crystal Solar Cells through Crystal Engineering and Weak Ion Migration. *Adv. Funct. Mater.* **2024**, *34* (32), 2313693.

(18) Turedi, B.; Lintangpradipto, M. N.; Sandberg, O. J.; Yazmaciyan, A.; Matt, G. J.; Alsalloum, A. Y.; Almasabi, K.; Sakhatskyi, K.; Yakunin, S.; Zheng, X.; et al. Single-Crystal Perovskite Solar Cells Exhibit Close to Half A Millimeter Electron-Diffusion Length. *Adv. Mater.* **2022**, *34* (47), 2202390.

(19) Chen, Y.-X.; Ge, Q.-Q.; Shi, Y.; Liu, J.; Xue, D.-J.; Ma, J.-Y.; Ding, J.; Yan, H.-J.; Hu, J.-S.; Wan, L.-J. General Space-Confined On-Substrate Fabrication of Thickness-Adjustable Hybrid Perovskite Single-Crystalline Thin Films. *J. Am. Chem. Soc.* **2016**, *138* (50), 16196−16199.

(20) Peng, W.; Wang, L.; Murali, B.; Ho, K.-T.; Bera, A.; Cho, N.; Kang, C.-F.; Burlakov, V. M.; Pan, J.; Sinatra, L.; et al. Solution-Grown Monocrystalline Hybrid Perovskite Films for Hole-Transporter-Free Solar Cells. *Adv. Mater.* **2016**, *28* (17), 3383−3390.
(21) Wang, Q.; Bai, D.; Jin, Z.; Liu, S. Single-crystalline perovskite wafers with a Cr blocking layer for broad and stable light detection in a harsh environment. *RSC Adv.* **2018**, *8* (27), 14848−14853.
(22) Chen, Z.; Dong, Q.; Liu, Y.; Bao, C.; Fang, Y.; Lin, Y.; Tang, S.; Wang, Q.; Xiao, X.; Bai, Y.; et al. Thin single crystal perovskite solar cells to harvest below-bandgap light absorption. *Nat. Commun.* **2017**, *8* (1), 1890.
(23) Yang, Z.; Xu, Q.; Wang, X.; Lu, J.; Wang, H.; Li, F.; Zhang, L.; Hu, G.; Pan, C. Large and Ultrastable All-Inorganic CsPbBr3Monocrystalline Films: Low-Temperature Growth and Application for High-Performance Photodetectors. *Adv. Mater.* **2018**, *30* (44), 1802110.
(24) Pratheek, M.; Chandra, G. K.; Predeep, P. Ultrathin single-crystalline perovskites: Toward large area wafers. *J. Cryst. Growth* **2022**, *597*, 126848.
(25) Deng, Y.-H.; Yang, Z.-Q.; Ma, R.-M. Growth of centimeter-scale perovskite single-crystalline thin film via surface engineering. *Nano Convergence* **2020**, *7* (1), 25.
(26) Feng, A.; Xie, S.; Fu, X.; Chen, Z.; Zhu, W. Inch-Sized Thin Metal Halide Perovskite Single-Crystal Wafers for Sensitive X-Ray Detection. *Front. Chem.* **2022**, *9*, 823868.
(27) Mahato, S.; Tamulewicz-Szwajkowska, M.; Singh, S.; Kowal, D.; Bose, S.; Serafińczuk, J.; Czyż, K.; Jędrzejewski, R.; Birowosuto, M. D.; Ray, S. K.; et al. Surface-Engineered Methylammonium Lead Bromide Single Crystals: A Platform for Fluorescent Security Tags and Photodetector Applications. *Adv. Opt. Mater.* **2024**, *12* (10), 2302257.
(28) Bhat, H. *Introduction to crystal growth: principles and practice*; CRC Press, 2014.
(29) Saidaminov, M. I.; Abdelhady, A. L.; Murali, B.; Alarousu, E.; Burlakov, V. M.; Peng, W.; Dursun, I.; Wang, L.; He, Y.; Maculan, G.; et al. High-quality bulk hybrid perovskite single crystals within minutes by inverse temperature crystallization. *Nat. Commun.* **2015**, *6* (1), 7586.
(30) Rudolph, P. *Handbook of crystal growth: Bulk crystal growth*; Elsevier, 2014.
(31) Stolterfoht, M.; Caprioglio, P.; Wolff, C. M.; Márquez, J. A.; Nordmann, J.; Zhang, S.; Rothhardt, D.; Hörmann, U.; Amir, Y.; Redinger, A.; et al. The impact of energy alignment and interfacial recombination on the internal and external open-circuit voltage of perovskite solar cells. *Energy Environ. Sci.* **2019**, *12* (9), 2778−2788.
(32) Wolff, C. M.; Caprioglio, P.; Stolterfoht, M.; Neher, D. Nonradiative Recombination in Perovskite Solar Cells: The Role of Interfaces. *Adv. Mater.* **2019**, *31* (52), 1902762.
(33) Chen, F.; Zhu, C.; Xu, C.; Fan, P.; Qin, F.; Gowri Manohari, A.; Lu, J.; Shi, Z.; Xu, Q.; Pan, A. Crystal structure and electron transition underlying photoluminescence of methylammonium lead bromide perovskites. *J. Mater. Chem. C* **2017**, *5* (31), 7739−7745.
(34) Marchioro, A.; Teuscher, J.; Friedrich, D.; Kunst, M.; van de Krol, R.; Moehl, T.; Grätzel, M.; Moser, J.-E. Unravelling the mechanism of photoinduced charge transfer processes in lead iodide perovskite solar cells. *Nat. Photonics* **2014**, *8* (3), 250−255.
(35) Shi, J.; Xu, X.; Li, D.; Meng, Q. Interfaces in Perovskite Solar Cells. *Small* **2015**, *11* (21), 2472−2486.
(36) Yadav, P.; Alotaibi, M. H.; Arora, N.; Dar, M. I.; Zakeeruddin, S. M.; Grätzel, M. Influence of the Nature of A Cation on Dynamics of Charge Transfer Processes in Perovskite Solar Cells. *Adv. Funct. Mater.* **2018**, *28* (8), 1706073.
(37) Stranks, S. D.; Eperon, G. E.; Grancini, G.; Menelaou, C.; Alcocer, M. J. P.; Leijtens, T.; Herz, L. M.; Petrozza, A.; Snaith, H. J. Electron-Hole Diffusion Lengths Exceeding 1 Micrometer in an Organometal Trihalide Perovskite Absorber. *Science* **2013**, *342* (6156), 341−344.
(38) Yuan, J.; Najmaei, S.; Zhang, Z.; Zhang, J.; Lei, S.; Ajayan, P. M.; Yakobson, B. I.; Lou, J. Photoluminescence Quenching and Charge Transfer in Artificial Heterostacks of Monolayer Transition Metal Dichalcogenides and Few-Layer Black Phosphorus. *ACS Nano* **2015**, *9* (1), 555−563.
(39) Li, C.; Zhong, Y.; Luna, C. A. M.; Unger, T.; Deichsel, K.; Gräser, A.; Köhler, J.; Köhler, A.; Hildner, R.; Huettner, S. Emission Enhancement and Intermittency in Polycrystalline Organolead Halide Perovskite Films. *Molecules* **2016**, *21* (8), 1081.
(40) Mehdi, H.; Matheron, M.; Mhamdi, A.; Cros, S.; Bouazizi, A. Effect of the hole transporting layers on the inverted perovskite solar cells. *J. Mater. Sci.: Mater. Electron.* **2021**, *32* (16), 21579−21589.
(41) Geng, X.; Liu, Y.; Zou, X.; Johansson, E. M. J.; Sá, J. Can photoluminescence quenching be a predictor for perovskite solar cell efficiencies? *Phys. Chem. Chem. Phys.* **2023**, *25* (34), 22607−22613.
(42) van Franeker, J. J.; Hendriks, K. H.; Bruijnaers, B. J.; Verhoeven, M. W. G. M.; Wienk, M. M.; Janssen, R. A. J. Monitoring Thermal Annealing of Perovskite Solar Cells with In Situ Photoluminescence. *Adv. Energy Mater.* **2017**, *7* (7), 1601822.
(43) Baloch, A. A. B.; Alharbi, F. H.; Grancini, G.; Hossain, M. I.; Nazeeruddin, M. K.; Tabet, N. Analysis of Photocarrier Dynamics at Interfaces in Perovskite Solar Cells by Time-Resolved Photoluminescence. *J. Phys. Chem. C* **2018**, *122* (47), 26805−26815.
(44) Mai, P.; Houel, J.; Dreveton, N.; Mahler, B.; Gassenq, A. High-Responsivity Planar Photodetector Based on Methylammonium Lead Bromide Perovskite Thin Film. *Photonics* **2023**, *10*, 1043.
(45) Sheng, R.; Ho-Baillie, A.; Huang, S.; Chen, S.; Wen, X.; Hao, X.; Green, M. A. Methylammonium Lead Bromide Perovskite-Based Solar Cells by Vapor-Assisted Deposition. *J. Phys. Chem. C* **2015**, *119* (7), 3545−3549.
(46) Fallah, K.; Norouzian Alam, S.; Ghaffary, B.; Yekekar, F.; Taghiyan, S.; Taravati, S. Enhancement of the environmental stability of perovskite thin films via AZ5214-photoresist and PMMA coatings. *Opt. Mater. Express* **2024**, *14* (8), 2083−2094.
(47) Fru, J. N.; Nombona, N.; Diale, M. Synthesis and characterisation of methylammonium lead tri-bromide perovskites thin films by sequential physical vapor deposition. *Phys. B* **2020**, *578*, 411884.

https://doi.org/10.1021/acsomega.4c09505
ACS Omega 2025, 10, 10220−10229